ACS APPLIED MATERIALS & INTERFACES

Research Article

www.acsami.org

Composite Magnetite and Protein Containing $CaCO_3$ Crystals. External Manipulation and Vaterite → Calcite Recrystallization-Mediated Release Performance

Alena Sergeeva,[*,†,‡] Roman Sergeev,[‡] Ekaterina Lengert,[‡] Andrey Zakharevich,[‡] Bogdan Parakhonskiy,[‡,§] Dmitry Gorin,[‡] Sergey Sergeev,[‡] and Dmitry Volodkin[†,‡]

[†]Fraunhofer Institute for Cell Therapy and Immunology (IZI), Am Muelenberg 13, 14467 Potsdam, Germany

[‡]Saratov State University, Astrakhanskaya 83, 410012 Saratov, Russia

[§]A.V. Shubnikov Institute of Crystallography, RAS, Leninskii prospekt 59, 119333 Moscow, Russia

Supporting Information

ABSTRACT: Biocompatibility and high loading capacity of mesoporous $CaCO_3$ vaterite crystals give an option to utilize the polycrystals for a wide range of (bio)applications. Formation and transformations of calcium carbonate polymorphs have been studied for decades, aimed at both basic and applied research interests. Here, composite multilayer-coated calcium carbonate polycrystals containing Fe_3O_4 magnetite nanoparticles and model protein lysozyme are fabricated. The structure of the composite polycrystals and vaterite → calcite recrystallization kinetics are studied. The recrystallization results in release of both loaded protein and Fe_3O_4 nanoparticles (magnetic manipulation is thus lost). Fe_3O_4 nanoparticles enhance the recrystallization that can be induced by reduction of the local pH with citric acid and reduction of the polycrystal crystallinity. Oppositely, the layer-by-layer assembled poly(allylamine hydrochloride)/poly(sodium styrenesulfonate) polyelectrolyte coating significantly inhibits the vaterite → calcite recrystallization (from hours to days) most likely due to suppression of the ion exchange giving an option to easily tune the release kinetics for a wide time scale, for example, for prolonged release. Moreover, the recrystallization of the coated crystals results in formulation of multilayer capsules keeping the feature of external manipulation. This study can help to design multifunctional microstructures with tailor-made characteristics for loading and controlled release as well as for external manipulation.

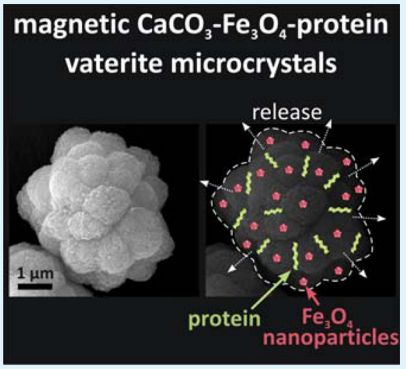

KEYWORDS: *calcium carbonate crystals, magnetite nanoparticles, coprecipitation, vaterite → calcite recrystallization, layer-by-layer assembly*

1. INTRODUCTION

At present, the development of composite nano- and microstructured materials with required properties is a promising direction in different fields of technology and engineering. A variety of new methods to fabricate nanoparticles,[1,2] multifunctional microcapsules,[3−5] and low-dimensional patterned structures[6−8] have been proposed. In recent years, calcium carbonate ($CaCO_3$) vaterite polycrystals are classified as advanced materials for biomedical and sensor applications due to their highly porous nature.[9−13] For encapsulation of (bio)active molecules based on vaterite templating, see the following works and reviews.[14−17] Together with biocompatibility, it stimulates the use of the crystals as a perfect system for encapsulation of molecules with low molecular weight, like photosensitizers,[18] doxorubicin,[19] as well as with high molecular weight, for example, dextran,[10,12] alginate,[12] catalase,[11] bovine serum albumin,[10,12] and insulin.[11,20,21] Integration of molecules of interest and functional materials such as nanoparticles (silver,[22] magnetite[23,24]) and nanotubes (halloysite,[25] carbon[26]) into the $CaCO_3$ crystals can be performed at mild conditions during the crystal growth (so-called coprecipitation)[5,27] as well as using the prepared crystals (filling of the mesopores by adsorption, solvent evaporation).[11,12,20] Moreover, layer-by-layer (LbL) assembly can be additionally applied to modify the surface of mesoporous calcium carbonate crystals with a multilayer shell consisting of macromolecules and/or functional compounds.[3,10,19,28−31] Functionalization of $CaCO_3$ vaterite (the internal structure or/and the surface of polycrystal) with inorganic nanoparticles makes them an effective platform for surface enhanced Raman microscopy,[22,32] sensitive to external stimuli such as electrical and magnetic fields, and light irradiation.[3,30,31,33] This opens new ways to manipulate/navigate with polycrystals and polymer capsules assembled on them (calcium carbonate can be easily dissolved at acidic pH),[34,35] for controlled release,

Received: June 30, 2015
Accepted: September 8, 2015
Published: September 8, 2015

DOI: 10.1021/acsami.5b05848
ACS Appl. Mater. Interfaces 2015, 7, 21315−21325

target delivery, and surface patterning[8] (e.g., using magnetic[6,36] or electric[7] fields).

The vaterite → calcite phase transition leads to a loss of the mesoporous vaterite internal structure (nonporous calcite polymorph is formed),[9,37−41] resulting in release of the vaterite-encapsulated additives from the pores of the crystals. Thus, the vaterite → calcite recrystallization process can be effective for release of encapsulated molecules.[9,18,42] The additives integrated into the internal $CaCO_3$ structure can provide not only new properties to vaterite crystals but also affect the recrystallization kinetics. It has been previously shown that vaterite → calcite recrystallization is a surface-controlled process, where the solubility of the calcium carbonate polymorphs and ion transport are key factors controlling growth of calcite.[40,41] Both factors depend on the surrounding media that affects the vaterite → calcite recrystallization and, as a consequence, the release kinetics.[18,42] In view of the above, we believe that it should be possible not only to use the vaterite → calcite transition as a release trigger[9,18,42] but also to control the release kinetics of (bio)molecules encapsulated into vaterite via coating of the crystals with a polyelectrolyte shell. The multilayers represent a polymer network with a high number of uncompensated permanent charges on polymer backbones that are compensated by counterions, which could be calcium and hydrocarbonate ions formed due to dissolution of $CaCO_3$ crystals.[43,44]A polyelectrolyte shell could effectively regulate ion transport on the crystal−liquid interface and thus affect the transformation rate of metastable vaterite to calcite. However, to the best of our knowledge, there is no study that considers such aspects.

In this work, we aim to design composite vaterite $CaCO_3$ crystals that can possess multiple functionalities, external manipulation and controlled release of crystal encapsulated compounds. Coprecipitation has been chosen as an effective method to encapsulate magnetite nanoparticles and protein molecules into the mesoporous internal volume of the vaterite crystals. LbL-assembled polyelectrolyte coating has been deposited onto the composite vaterite $CaCO_3$ crystals with the aim to control the vaterite → calcite recrystallization rate and, as a result, the protein release kinetics. The vaterite/calcite ratio has been used as an indicator of these release kinetics. Internal structure of the crystals and kinetics of the vaterite → calcite recrystallization have been examined using scanning electron microscopy (SEM), X-ray diffraction (XRD), and confocal laser scanning microscopy (CLSM).

2. EXPERIMENTAL SECTION

2.1. Materials. The following materials were used in this study: poly(allylamine hydrochloride) (PAH, MW 70 kDa, Sigma), poly(sodium styrenesulfonate) (PSS, MW 70 kDa, Sigma), calcium chloride dihydrate ($CaCl_2$, Serva), sodium carbonate (Na_2CO_3, Reahim), sodium hydroxide (NaOH, Ekros), iron chloride(II) ($FeCl_2$, Panreac), iron chloride(III) ($FeCl_3$, Vekton), citric acid ($C_6H_8O_7$, Alfa Aesar GmbH & Co KG), phosphate buffer saline tablets (PBS, Sigma-Aldrich), Trizma base (TRIS, Primary Standard and Buffer, ≥99.9% (titration), crystalline, Sigma), FITC-lysozyme (MW 14.3 kDa, Sigma), and alginic acid sodium salt from macrocystis pyrifera (MW 12−80 g mol^{-1}, viscosity of 2% solution at 25 °C approximately 250 cps, plant cell culture tested, Sigma-Aldrich). All of the chemicals were used as purchased without further purification; all of the solutions were prepared using Millipore water produced in a three-stage Millipore Milli-Q Plus 185 purification system and having a resistivity higher than 18.2 MΩ cm.

2.2. Synthesis of Fe_3O_4 Nanoparticles. Suspensions of Fe_3O_4 nanoparticles were synthesized on the basis of a standard chemical precipitation method using salt solutions of ferrous and ferric iron.[45−47] $FeCl_3$ (1.2 g) and $FeCl_2$ (0.5 g) were dissolved at room temperature in 20 mL of Millipore water with constant stirring by a magnetic stirrer (Mini MR Standard rotor stirrer, IKAMAG, Germany). The prepared solution of the salts was rapidly injected under vigorous stirring into sodium hydroxide solution (180 mL of 0.1 M NaOH solution) under a nitrogen atmosphere and left under stirring for 30 min under a nitrogen atmosphere. The resulting black sediment of the formed Fe_3O_4 nanoparticles was collected from the solution using a permanent magnet (pull off force 70 N) and sequentially washed three times with 25 mL of citric acid (20 mg mL^{-1}). Dialysis (3 days) was performed for the concentrated colloid of the stabilized Fe_3O_4 nanoparticles. Resulting nanoparticles were stored at 4 °C.

To fabricate the Fe_3O_4 nanoparticles of different sizes, the following conditions (or materials) can be adjusted: temperature of the solutions used, agitation rate, the use of a stabilizer/additive, and concentration of initial salts used. In this work, the temperature was constant (25 °C), and water was used as a solvent for all of the procedures described. The as-prepared colloids were always stabilized with citric acid (three rinses with 25 mL of citric acid at a concentration of 20 mg mL^{-1}). The agitation rate was the only parameter changed; higher agitation rate was applied to produce smaller nanoparticles by variation of the stirring rate from 150 to 500 rpm.

The hydrodynamic diameter and ζ-potential of the Fe_3O_4 nanoparticles produced were calculated from dynamic light scattering measurements (Table S1, Figure S1); shape and size distribution of the nanoparticles were additionally examined by analysis of scanning electron microscopy and transmission electron microscopy images. The concentration of Fe_3O_4 nanoparticles was determined by weighting of the dried sample and was found to be in the range 5−15 mg mL^{-1}. The concentration of citric acid in the colloids was found to be 0.3 mg mL^{-1} when assuming that the stabilizer coating represents a monolayer of organic molecules on the surface of Fe_3O_4 nanoparticles of a certain determined size.

2.3. Fabrication of $CaCO_3$ Vaterite Crystals. Calcium carbonate vaterite crystals with and without Fe_3O_4 nanoparticles were fabricated on the basis of the previously established coprecipitation approach[10,11] as described below. All of the solutions and procedures described were performed at room temperature.

To produce composite $CaCO_3$−Fe_3O_4 vaterite crystals, the suspension of Fe_3O_4 in water (2.5 mL, concentrations in the range of 0.05−1.35 mg mL^{-1}) was constantly stirred at an agitation speed of 160 rpm in a glass beaker with a total volume of 10 mL. Equal volumes (625 μL) of 1 M Na_2CO_3 and 1 M $CaCl_2$ salts were simultaneously added to the beaker with the Fe_3O_4 nanoparticles. The resulting suspension was stirred for 30 s inducing nucleation of calcium carbonate vaterite crystals, followed by incubation for another 1−3 min (no stirring) to complete the crystal growth. Note that the temperature of the solutions used and the agitation speed and time have been kept constant (25 °C, 160 rpm, and 30 s, respectively) for all of the experiments to provide identical conditions for $CaCO_3$−Fe_3O_4 vaterite crystallization. The prepared $CaCO_3$−Fe_3O_4 crystals were quickly rinsed with Millipore water (three times) followed by air-drying at 70 °C for 30 min. The dried $CaCO_3$−Fe_3O_4 crystals were stored at room temperature in Eppendorf microtubes. In this way, the composite $CaCO_3$−Fe_3O_4 crystals containing 0.125−3.000 mg (0.03−0.72 M) of Fe_3O_4 nanoparticles were produced (Table S1). The yield of $CaCO_3$−Fe_3O_4 crystals for the above-described approach was always 50−55 mg, with the content of vaterite in the range of 96−99% (evident from SEM and optical transmittance images, and XRD analysis).

To study how Fe_3O_4 nanoparticles coprecipitated with calcium carbonate affected vaterite crystallization, the reference $CaCO_3$ crystals without magnetite were fabricated by the methods described above. All of the procedures and conditions were the same except for the very first step: 2.5 mL of Millipore water instead of Fe_3O_4 suspension was used to prepare the reference $CaCO_3$ crystals. The yield of $CaCO_3$−

DOI: 10.1021/acsami.5b05848
ACS Appl. Mater. Interfaces 2015, 7, 21315−21325

Fe_3O_4 crystals was in the range of 50−55 mg, where the content of calcite polymorph did not exceed 4%.

2.4. Encapsulation of Protein into $CaCO_3$−Fe_3O_4 Vaterite. Loading of composite $CaCO_3$−Fe_3O_4 crystals with protein was performed using two approaches, coprecipitation[5,27] and solvent evaporation.[11,12,20] In both approaches, all of the solutions used and all of the reactions performed during loading were at room temperature.

In the case of loading by coprecipitation, FITC-lysozyme was integrated into the internal structure of vaterite together with Fe_3O_4 nanoparticles. In a glass beaker (total volume 10 mL), FITC-lysozyme (1 mL of 1 mg mL^{-1} solution in 100 mM TRIS contained 15 mM NaCl) was mixed with Fe_3O_4 nanoparticles (1.5 mL of 1 mg mL^{-1} suspension in water). The resulting suspension was stirred using a magnetic stirrer, and equal volumes of Na_2CO_3 and $CaCl_2$ (0.625 mL of 1 M solutions) were simultaneously added to the beaker. The suspension was mixed during 15 s (agitation speed 160 rpm) followed by incubation at room temperature for 3 min. The resulting crystals were rinsed with Millipore water three times and air-dried at 70 °C over 30 min. The yield of the composite $CaCO_3$−Fe_3O_4 polycrystals loaded with FITC-lysozyme was about 50 mg.

To load crystals with protein by means of solvent evaporation, 20 mg of the prepared $CaCO_3$−Fe_3O_4 crystals was dispersed in 2 mL of 1 mg mL^{-1} FITC-lysozyme solution in water. The suspension was shaken for 15 min followed by dropping onto the glass substrate and drying at 70 °C over 30 min.

2.5. Assembly of the Multilayer Polyelectrolyte Shell. The polyelectrolyte multilayers were adsorbed on the surface of the prepared composite $CaCO_3$−Fe_3O_4 and reference $CaCO_3$ crystals using LbL assembly.[28] PAH and PSS polyelectrolytes were used as polycationic and polyanionic components, respectively. The assembly of the shell was always started with the positively charged polyelectrolyte and finished with the negatively charged one. To deposit the first layer, vaterite crystals were mixed with the PAH solution (1 M NaCl solution, 2 mg mL^{-1}). The suspension was shaken for 15 min followed by the three rinses with Millipore water to remove unreacted constituents. The second layer was deposited by adsorption of the anionic component. Vaterite crystals coated with PAH were dispersed in the PSS solution (1 M NaCl solution, 2 mg mL^{-1}). After 15 min of shaking, three rinsing steps were performed. In this way, the vaterite crystals were covered with one (PAH/PSS) bilayer. The alternative deposition of the oppositely charged polyelectrolytes was repeated in the same way n times to assemble $(PAH/PSS)_n$ bilayers (where n was 1, 3, or 5). Control over the LbL-assembly was performed for each adsorbed layer by measurements of the electrokinetic potential value (Figure S3).

2.6. Vaterite → Calcite Recrystallization. The experiments to study the kinetics of the vaterite → calcite recrystallization were performed for both the composite $CaCO_3$−Fe_3O_4 crystals and the reference $CaCO_3$ vaterite (to reveal the effect of Fe_3O_4 nanoparticles on the recrystallization). The crystals (10 mg) were immersed in water (2 mL); the Eppendorf microtubes were vortexed at room temperature during the experiments. The suspensions were dripped (20 μL of suspension per drop) onto ethanol-precleaned silicon wafers every 1 h followed by air-drying at room temperature. The dropping was continued for 2 days to obtain a sequence of dried drops possessing various ratios of vaterite and calcite. The experiments were repeated three times. The following SEM measurements provided visual tracking of the vaterite → calcite recrystallization for the composite $CaCO_3$−Fe_3O_4 and the reference $CaCO_3$ crystals. Statistical image analysis (recrystallization kinetics) was performed using ImageJ (NIH) based on n = 100 crystals per sample.

To study an influence of the ion transport in the near-surface area of vaterite crystals on the vaterite → calcite recrystallization, the above-described experiment was performed for the composite $CaCO_3$−Fe_3O_4 and the reference $CaCO_3$ crystals covered with $(PAH/PSS)_n$ polyelectrolyte shell (n is 1,3,5). For these experiments, the time interval between deposition of each drop of the suspensions was equal to 24 h. The different drip time (24 h instead of 1 h) was chosen on the basis of the assumption that the polyelectrolyte shell could inhibit the ion transport providing slower recrystallization.

2.7. Recrystallization-Mediated Release of Protein. FITC-lysozyme was encapsulated into the composite $CaCO_3$−Fe_3O_4 crystals by coprecipitation together with Fe_3O_4 nanoparticles as described above (section 2.4). To investigate the recrystallization-mediated release, FITC-lysozyme-loaded $CaCO_3$−Fe_3O_4 crystals (10 mg) were resuspended in water (2 mL) and incubated at room temperature in carefully sealed Eppendorf centrifuge tubes. After different incubation times, the samples were centrifuged, and a drop of supernatant (2 μL) solution was taken from the suspension. To obtain the recrystallization-mediated release kinetics, absorbance at 494 nm was detected using a Thermo Scientific NanoDrop 1000 spectrophotometer (Thermo Fisher Scientific, U.S.). To determine the absolute values of protein released, a calibration curve based on known concentrations was used.

2.8. Dynamic Light Scattering (DLS). DLS measurements were performed using a Malvern Zetasizer Nano ZS Setup (Malvern Instruments Ltd., England) to examine ξ-potential and average size distribution (hydrodynamic diameter) of the Fe_3O_4 nanoparticles. For these measurements, the suspensions of particles in water of concentration 0.1 mg mL^{-1} were used. Measurements of hydrodynamic diameter (particle size) were performed at 25 °C using disposable cuvettes (UV-Cuvette Micro 759200) of 70 μL volume (Brand GMBH, Germany). For each sample, a series of 10 runs was done. ξ-Potential was determined using disposable folded capillary cells DTS1070 (Zetasizer Nano Series, Malvern, UK), and the resulting values were an average of three measurements. In the same manner, ξ-potential of the composite $CaCO_3$−Fe_3O_4/$(PAH/PSS)_n$ was determined after deposition of each polyelectrolyte layer using Malvern Zetasizer 4 (Malvern Instruments Ltd., England).

2.9. Transmission Electron Microscopy (TEM). The measurements were conducted on a Zeiss EM 912 Omega transmission electron microscope (Zeiss, Germany). An aqueous colloidal solution of Fe_3O_4 nanoparticles was dropped onto the carbon-coated copper grids, and the grids were then dried at room temperature.

2.10. Scanning Electron Microscopy (SEM). These measurements were performed using MIRA II LMU installation (TESCAN, Czech Republic) to characterize the fabricated vaterite microcrystals (shape, size, porosity, and surface morphology). Ultramicrotome Leica EM UC7 (Leica, Germany) was used to prepare the ultrathin sections of crystals to examine the internal structure of the crystals produced. For SEM measurements, the water suspension of calcium carbonate crystals (20 μL) was dropped onto the silicon wafer and air-dried at room temperature. Prior to the measurement, the samples were sputtered with gold. Measurements were performed at an operating voltage of 3−30 keV. Statistical image analysis (crystal size distributions and amount of raspberry-shaped and spherical vaterite in the samples) was performed using ImageJ (NIH) based on n = 100 crystals per sample.

Elementary composition analysis (ECA) was performed using the same MIRA II LMU installation to examine the composition of the composite $CaCO_3$−Fe_3O_4/$(PAH/PSS)_n$ crystals at different time intervals during the recrystallization. The area of interest of 1−3 μm^2 was chosen in situ (e.g., a part of $(PAH/PSS)_5$ crystal, or an empty $(PAH/PSS)_n$ capsule), and the ECA provides the list of elements (with a percentage) contained in the chosen area.

2.11. X-ray Diffraction (XRD). Measurements were performed to confirm the vaterite → calcite recrystallization kinetics estimated from SEM as described in the previous paragraph. On the basis of the recrystallization kinetics, three time periods were chosen to perform XRD measurements, 0 h after the recrystallization was started (almost all of the crystals should be vaterite), 20 h (crystals have to be mixed vaterite and calcite phase), and 40 h (almost all of the crystals have become calcite).

The samples of the composite $CaCO_3$−Fe_3O_4 and the reference $CaCO_3$ crystals were prepared for XRD measurements as follows. The suspensions of the crystals in water were prepared at a concentration of 1 mg mL^{-1} and kept at room temperature for the corresponding time (0, 20, or 40 h). The supernatant solution then was removed, and the crystals were air-dried at 90 °C for 1 h. The XRD data were obtained using a Gemini A Ultra X-ray Diffraction System (Agilent

DOI: 10.1021/acsami.5b05848
ACS Appl. Mater. Interfaces 2015, 7, 21315−21325

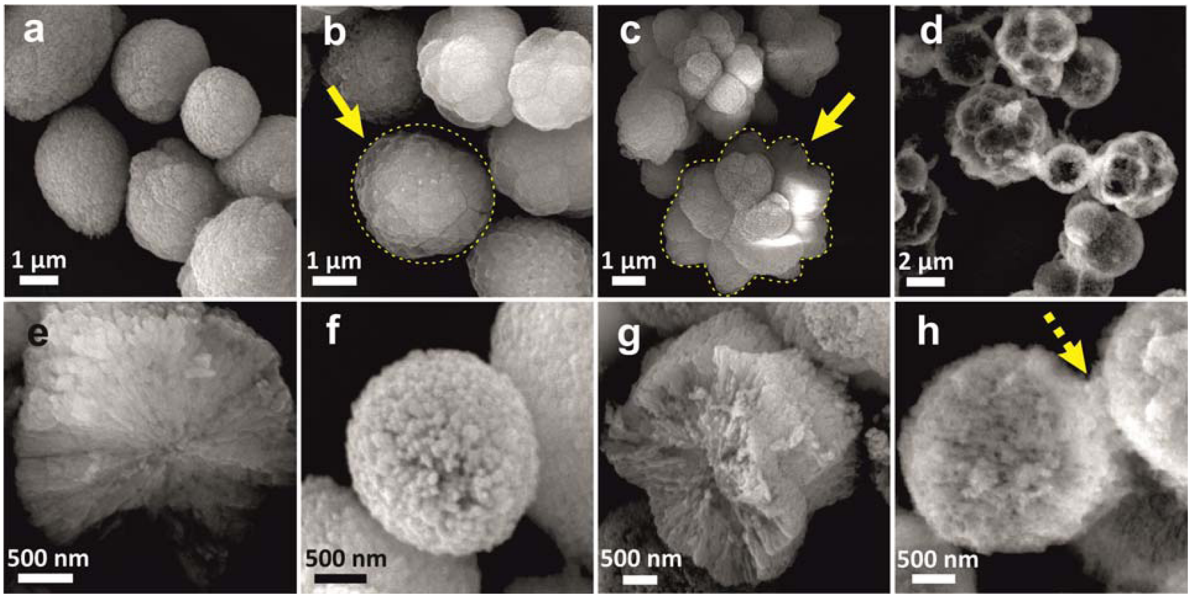

Figure 1. SEM images showing (a,e) the reference magnetite-free $CaCO_3$ vaterite crystals and the composite $CaCO_3$–Fe_3O_4 crystals fabricated using various concentrations of Fe_3O_4 nanoparticles (average size 34 nm; ζ-potential −17 mV). Ratios of $CaCO_3$ to Fe_3O_4 were as (b,f) 500:1; (c,g) 50:1; and (d,h) 5:1. Yellow solid arrows and interrupted lines in (b) and (c) are provided to indicate spherical and raspberry-shaped vaterite crystals. The dotted arrow in (h) points out the bridge aggregation of the formed $CaCO_3$–Fe_3O_4 crystals.

Technologies, U.S.), with a source of Cu Kα. The XRD data obtained were compared to the literature crystallographic data reported by le Bail[48] and Sitepu[49] for vaterite and calcite, respectively. The calcite and vaterite crystallite sizes were estimated by the Scherrer equation[50,51] based on the three most intense peaks for each phase.

2.12. Confocal Laser Scanning Microscopy (CLSM). This was used to examine the distribution of the encapsulated vaterite FITC-lysozyme over the internal structure of $CaCO_3$–Fe_3O_4 crystals. CLSM images were obtained using a Zeiss LSM 510 Meta installation (Zeiss, Germany). An oil-immersion objective with 63× magnification and numerical aperture of 1.4 was used. Standard filter settings for excitation and emission of FITC were used for the laser sources with wavelengths of 488 and 633 nm. All of the CLSM experiments were performed at room temperature. Analysis of the CLSM images has been done by means of ImageJ and LSM Image Browser. The fluorescence profiles taken from the CLSM images were plotted using Microsoft Excel software.

3. RESULTS AND DISCUSSION

3.1. Crystallization of the Composite $CaCO_3$–Fe_3O_4 Crystals. To examine the effect of magnetite nanoparticles on the crystallization of $CaCO_3$ vaterite, Fe_3O_4 nanoparticles with average hydrodynamic radii from 19 ± 7 to 82 ± 16 nm (Table S1) were synthesized on the basis of the approach previously established by Rene Massart.[45−47] Magnetic $CaCO_3$–Fe_3O_4 polycrystals were fabricated using coprecipitation as described in the Experimental Section, with variation of the Fe_3O_4 nanoparticle contents and the nanoparticle sizes to examine the influence of these parameters on the characteristics of the $CaCO_3$ crystals produced.

To demonstrate the magnetic properties of the $CaCO_3$–Fe_3O_4 crystals, an external magnetic field induced by a permanent magnet (a pull off force 70 N, magnetic induction vector 0.3 T) was applied to the crystals dispersed in water (viscosity about 1 cP at 25 °C). The prepared $CaCO_3$–Fe_3O_4 crystals were manipulated by magnetic field even when the lowest examined concentration of Fe_3O_4 nanoparticles was coprecipitated in vaterite (mass ratio of $CaCO_3$ to Fe_3O_4 as 900 to 1). Crystals demonstrated the immediate response to the external magnetic field applied. To examine the possibility of manipulation in viscous media, $CaCO_3$–Fe_3O_4 crystals were dispersed in concentrated sodium alginate solution in water (viscosity about 250 cP for 2% H_2O solution at 25 °C). As expected, an average rate of crystal movement (determined visually from the time needed for $CaCO_3$–Fe_3O_4 crystals placed in media to cover a distance of 1 cm) was significantly decreased, dropping from 3.3×10^{-1} in water to 1.6×10^{-2} cm s^{-1} in 3% sodium alginate solution. However, $CaCO_3$–Fe_3O_4 crystals were still manipulated in viscous media. Control experiments with the reference magnetite-free $CaCO_3$ vaterite showed no response of the crystals to the external magnetic field at the same conditions. Thus, integration of Fe_3O_4 nanoparticles into the internal structure of $CaCO_3$ provided the crystals with magnetic properties.

SEM images of the produced crystals have revealed the pronounced effect of Fe_3O_4 nanoparticles on the structure of the $CaCO_3$ formed (Figure 1, Table S2). Interestingly, addition of Fe_3O_4 nanoparticles during calcium carbonate coprecipitation did not result in a change of the typical highly porous vaterite structure[10,11,13,20,52] (Figure 1g) but caused the changes in shape and morphology, which are dependent on the content of nanoparticles (Figure 1b–d,f–h). While magnetite-free $CaCO_3$ crystals are mainly spherical (~80% by number), the composite $CaCO_3$–Fe_3O_4 crystals prepared at the same conditions possess primarily (up to 70%) a raspberry-like shape as shown in Figure 1c. For crystals produced at identical conditions, the average diameter of $CaCO_3$–Fe_3O_4 raspberry-vaterite was 4.5 ± 1.0 μm, almost 80% larger than the size of spherical magnetite-free $CaCO_3$ vaterite (Figure 1a,b). The designed composite $CaCO_3$–Fe_3O_4 vaterite crystals possess a highly developed surface and can be manipulated by an external magnetic field. Both features make them attractive for encapsulation and controlled delivery of (bio)molecules.

The $CaCO_3$–Fe_3O_4 crystals fabricated are rather polydisperse for all of the examined Fe_3O_4 nanoparticles (examples of crystals are shown in Figure S2) that is typical for the

DOI: 10.1021/acsami.5b05848
ACS Appl. Mater. Interfaces 2015, 7, 21315−21325

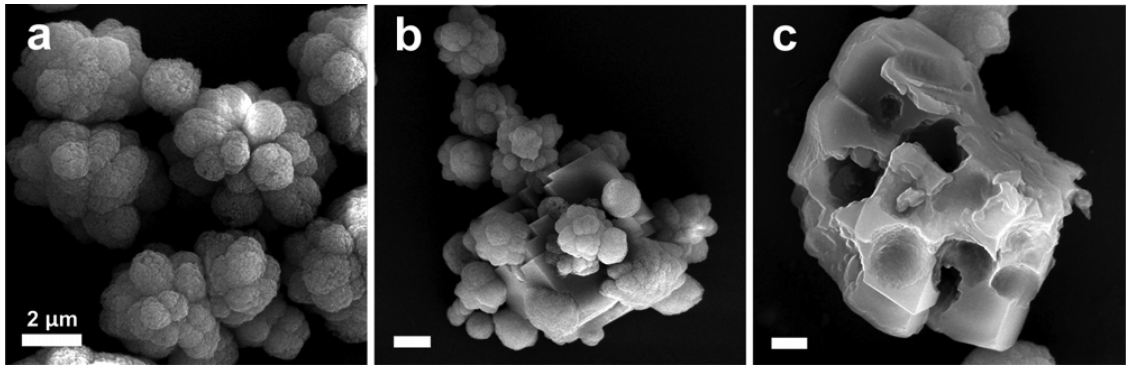

Figure 2. SEM images of uncoated $CaCO_3$−Fe_3O_4 vaterite crystals prepared using a 1 mg mL^{-1} suspension of Fe_3O_4 nanoparticles (average size 34 nm; ζ-potential −17 mV) after (a) 1, (b) 10, and (c) 26 h after synthesis. Scale bars are 2 μm for all of the images.

precipitated calcium carbonate. However, the analysis of the composite $CaCO_3$−Fe_3O_4 vaterite has revealed the following dependence. The higher is the content of Fe_3O_4 nanoparticles coprecipitated in $CaCO_3$, the larger is an average size of the $CaCO_3$−Fe_3O_4 raspberry crystals and the higher is their total number in the sample (Table S1). The trends observed in the formation of raspberry crystals can be explained by heterogeneous nucleation taking place in coprecipitation of calcium carbonate.[11,53−55] Despite its relevance, little is known about the $CaCO_3$ precipitation mechanism. In the classic theory, nucleation is considered to take place when saturated solutions of sodium carbonate and calcium chloride are mixed, leading to a nucleation of a solid phase via stochastic solute clustering. The earliest crystal precursor is considered to be a cluster of critical size: once a critical point is reached, a cluster becomes thermodynamically able to grow by single-ion precipitation.[54] According to the novel view, there exists a prenucleation stage at first, when stable clusters with a size of ∼2 nm (about 70 calcium and carbonate ions) are formed.[54] In the early postnucleation stage, crystal species of 5−6 nm were detected, while smaller clusters disappeared. By this theory, nucleation is a cluster aggregation (not only a precipitation of single ions).[54] When the critical size is reached, amorphous calcium carbonate (ACC) precipitates at first.[53,54] Amorphous $CaCO_3$ crystallizes to vaterite via a three-stage process described in detail by Bots et al.[53] The hydrated ACC nucleated at supersaturated conditions becomes dehydrated with the concurrent increase of local order. This provides nucleation and spherulitic growth of vaterite via aggregation of the clusters presented in the saturated solution (taking place as long as highly soluble ACC is present in the system). Once all of the ACC clusters are consumed, vaterite continues to grow via Ostwald ripening (dissolution/precipitation processes).[53] The size and the number of the resulting $CaCO_3$ vaterite crystals depend on the concentration of clusters nucleated. The number of the formed nuclei can be increased if one uses a faster stirring rate, longer stirring time, higher temperature, or additives such as (bio)macromolecules (proteins, polysaccharides, dyes)[11,56] and inorganic nanoparticles.[55] According to the Ostwald rule, Fe_3O_4 nanoparticles and proteins mixed with saturated salt solutions act as additional nucleation centers because metastable vaterite phase tends to precipitate at a higher local supersaturation (around the additive).[53−56] In this way, higher concentrations of additives provide more nucleation centers for calcium carbonate crystallization. On the other hand, high concentration of the growing nuclei induces their frequent contact with each other (due to stirring of the suspension) leading to simultaneous growth of connected (fused) crystals. Formation of such aggregated vaterite has been previously observed for the nanosized crystals coprecipitated in the presence of ethylene glycol[56] and for hundred micrometer-sized particles formed in the presence of a block copolymer containing poly(ethylene glycol)-*b*-poly(aspartic acid).[57]

This can explain the increased yield of $CaCO_3$−Fe_3O_4 raspberry crystals (up to about 70%) when a higher concentration of the Fe_3O_4 nanoparticles was used. Low concentration of Fe_3O_4 nanoparticles (molar ratio of $CaCO_3$ to Fe_3O_4 less than 500 to 1) provided an insufficient amount of nuclei to cause formation of raspberry crystals; magnetic $CaCO_3$−Fe_3O_4 vaterite with a quasispherical shape was formed (Figure 1b,f). Very high concentrations of Fe_3O_4 nanoparticles (molar ratio of $CaCO_3$ to Fe_3O_4 as 5 to 1) caused a bridge aggregation of the grown $CaCO_3$−Fe_3O_4 crystals (Figure 1d,h; the junction between the aggregated crystals is indicated with the yellow dotted arrow). Such high nanoparticle concentrations can also result in a blocking of the pores of $CaCO_3$−Fe_3O_4 vaterite crystals, thus limiting the use of the crystals for loading/release of molecules of interest.

3.2. Recrystallization of the Uncoated $CaCO_3$−Fe_3O_4 Vaterite. Kinetics of vaterite → calcite recrystallization was studied for both the reference magnetite-free $CaCO_3$ and the composite $CaCO_3$−Fe_3O_4 crystals to examine the effect of Fe_3O_4 nanoparticles on the vaterite stability. Vaterite → calcite recrystallization consists of the dissolution of metastable vaterite phase (decomposition into ions) accompanied by the growth of calcite (Figure 2). As evidenced by the SEM images that captured the recrystallization, the first calcite crystals appeared after about 2 h of storage in water and primarily in places with the highest density of $CaCO_3$ (e.g., between several vaterite crystals contacting each other, Figure 3b) where the released ions are in excess. These singular calcite nuclei induced first the dissolution of the nearby vaterite, which provide ions for calcite growth. As a result, the neighbor vaterite crystals recrystallized to a "complex" calcite monocrystal with dimensions of tens micrometer (Figure 2c). The vaterite crystals that separated in space recrystallized to calcite later (i) via dissolution followed by ion reprecipitation on the nearest surfaces of big calcite crystals, or (ii) via in situ transformation to a single calcite. The observations above are in line with literature findings that show that the surface of growing calcite determines the rate of recrystallization.[37,38,40,53]

The recrystallization mechanism of $CaCO_3$ and $CaCO_3$−Fe_3O_4 vaterite has been found to be of similar nature. For both

DOI: 10.1021/acsami.5b05848
ACS Appl. Mater. Interfaces 2015, 7, 21315−21325

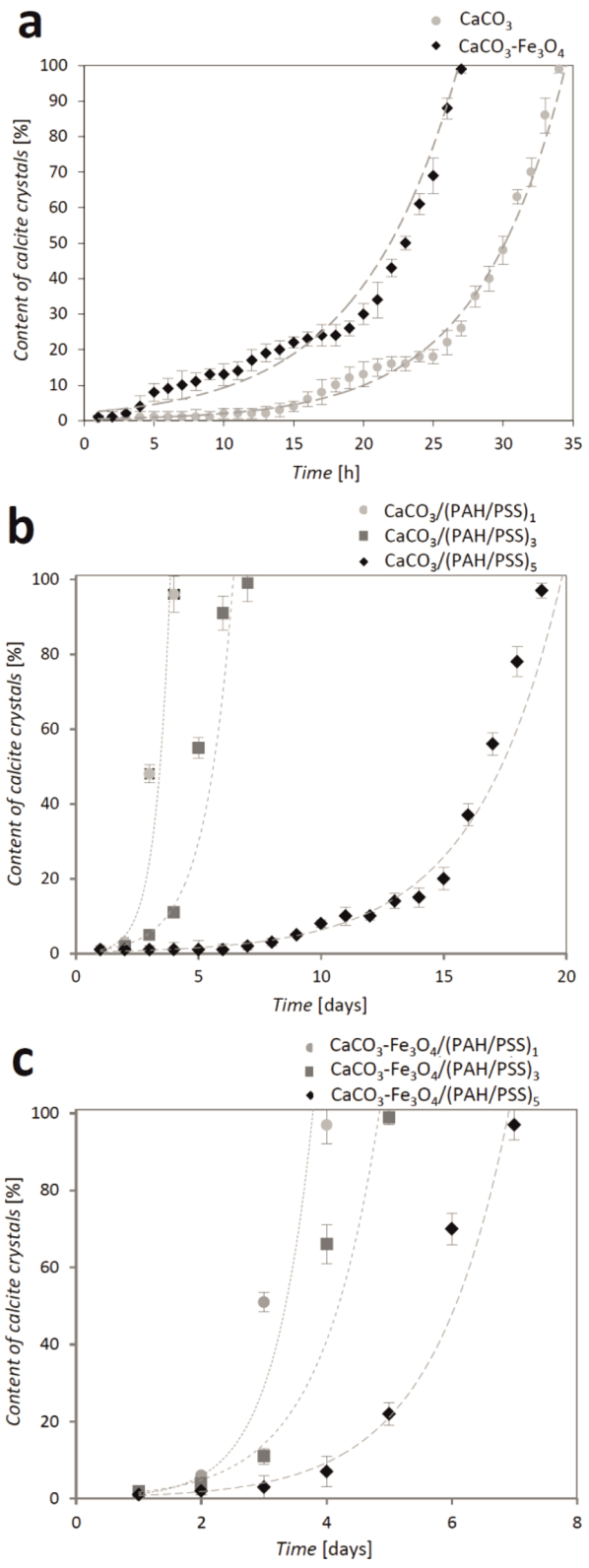

Figure 3. Content of calcite crystals as a function of time for (a) uncoated $CaCO_3$ and $CaCO_3$–Fe_3O_4 vaterite and for (b,c) vaterite coated with $(PAH/PSS)_n$ polyelectrolyte shell (n is 1,3,5). $CaCO_3$–Fe_3O_4 crystals were prepared using 1 mg mL^{-1} Fe_3O_4 colloid (average size 34 nm; ζ-potential −17 mV). $CaCO_3$–Fe_3O_4/$(PAH/PSS)_n$ crystals were produced using 1 mg mL^{-1} Fe_3O_4 colloid (average size 70 nm; ζ-potential −27 mV) (Table S1). The interrupted lines are the trend lines plotted for the data points obtained to guide the eye.

types of crystals, the dependence of calcite content as a function of time exhibits exponential behavior (Figure 3a). The recrystallization data obtained for the reference $CaCO_3$ can be fitted by the following equation: $y = 0.41\ e^{0.16x}$ (the squared correlation coefficient R^2 is 0.97). For recrystallization of the composite $CaCO_3$–Fe_3O_4 vaterite, the best fitting has been done using the equation: $y = 2.26\ e^{0.14x}$ (R^2 is 0.88). As is evident in Figure 3a, the functions have two well-defined sections, indicating slow and burst recrystallization. Magnetite-free $CaCO_3$ crystals kept vaterite modification for a significantly long time (maximum 2% of calcite phase after 12 h), while recrystallization of the composite $CaCO_3$–Fe_3O_4 crystals began almost immediately after the synthesis (18% of calcite by the 12th hour). Besides this lag-time (0–12th hour), recrystallization of the reference magnetite-free $CaCO_3$ is similar to that for the composite $CaCO_3$–Fe_3O_4 vaterite.

The exponential behavior observed (Figure 3a) can be explained by the fact that vaterite → calcite recrystallization is both a surface-determined and a solution-mediated process.[37,38,40,53] The vaterite phase has been kept when $CaCO_3$ crystals are in a dry state or placed in nonpolar solvent such as ethanol; however, vaterite transforms into calcite when dispersed in water-based solution.[42] Metastable vaterite dissolves into ions, which reprecipitate onto the surfaces of stable calcite. Dissolution/precipitation processes are called surface-determined because they involve the ion exchange taking place on the active surfaces of crystals. The higher is the total vaterite surface is, the faster is the dissolution process (more ions are released per unit time). In the same way, the larger is the calcite total surface, the faster is the precipitation (more ions are adsorbed). Indeed, new calcite crystals are constantly formed due to the in situ recrystallization of vaterite. At the same time, the calcite phase is growing due to enlargement of the already existing calcite surfaces. As a result, the vaterite → calcite recrystallization goes faster if more calcite is presented in the suspension that represents the exponential-like recrystallization profile (Figure 3a).

On the basis of the recrystallization kinetics obtained (Figure 3a), three time intervals (0, 20, and 40 h after the synthesis of crystals) were chosen to perform XRD measurements to identify the crystallinity of $CaCO_3$ (vaterite or calcite) at the determined recrystallization time and to define the approximate percentage of the corresponding phase in the sample.[58,59] The measurements at 0 and 40 h should give spectra of only pure vaterite and pure calcite, respectively. The middle point (20 h) should show a superposition spectrum in which both vaterite and calcite are present in the samples.

The spectra obtained (Figure 4) are in a good agreement with the literature data; all of the peaks observed correspond to vaterite or calcite.[48,49,58,59] Note that the aragonite phase has never been observed in the calcium carbonate crystals fabricated,[60] most probably due to the synthesis and recrystallization of $CaCO_3$ performed at low temperatures (aragonite appears at higher temperature or pressure).[53,56] As can be seen from the deconvoluted XRD data obtained for the composite $CaCO_3$–Fe_3O_4 crystals (Figure S4), 111 plane of aragonite does not merge. There are no characteristic peaks at 2θ of 26.213° and 27.216°, and the other strong peak of aragonite at 45.853° is also not observed, pointing to the absence of aragonite phase in the calcium carbonate crystals produced. Indeed, the highly intensive vaterite peaks corresponding to the (020), (110), (120), (220), and (211) Miller index of vaterite (Bragg peaks at 23.9°, 27.0°, and 32.8°)

DOI: 10.1021/acsami.5b05848
ACS Appl. Mater. Interfaces 2015, 7, 21315–21325

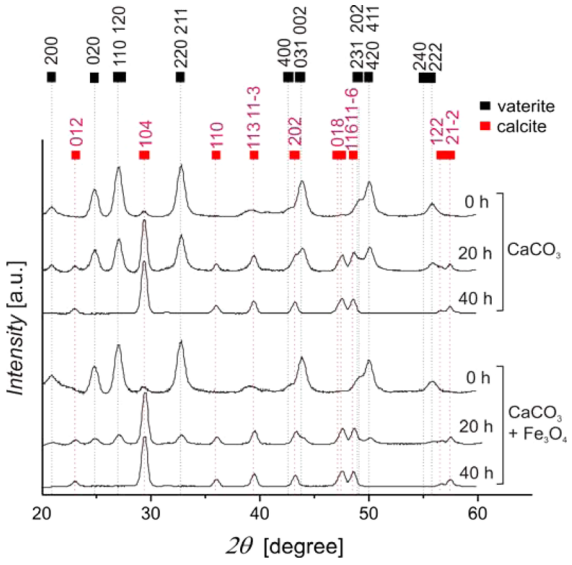

Figure 4. XRD data obtained for the reference $CaCO_3$ and the composite $CaCO_3$–Fe_3O_4 crystals obtained for the crystals incubated for 0, 20, and 40 h at 25 °C. Peaks indicated with black and red squares correspond to vaterite and calcite phases, respectively.

are present on the graphs at 0 and 20 h, but they disappear after 40 h, when the sample became definitively calcite as shown by SEM (Figure 2c). In the same way, the indicative peaks of calcite that corresponded to the (104), (110), (113), and ($11\bar{3}$) calcite crystalline planes (Bragg peaks at 29.4°, 36.0°, 39.4°) have low intensity on the spectra at 0 h, but are significantly (10 times) increased at 20 h. This demonstrates the increase of the calcite content from negligible initially (at 0 h) to the dominant phase after 20 h. The XRD data obtained after 40 h demonstrate only strong peaks related to calcite phase meaning that all of the crystals became calcite by that time.

XRD analysis performed for crystals incubated for 20 h demonstrated the indicative peaks of both vaterite and calcite phases indicating partial vaterite → calcite recrystallization. According to these data, different peak intensities are observed for reference $CaCO_3$ and composite $CaCO_3$–Fe_3O_4 crystals that can be explained by different rates of vaterite → calcite recrystallization. For the reference Fe_3O_4-free sample, less than 60% of $CaCO_3$ crystals became calcite by the 20th hour; this value is 80% for the composite $CaCO_3$–Fe_3O_4 crystals, indicating faster vaterite → calcite recrystallization for Fe_3O_4-containing vaterite (in line with the recrystallization kinetics extracted from the SEM data, Figure 3a).

The crystallite sizes of the crystals have been estimated by the Scherrer equation on the basis of the three most intensive vaterite peaks for each spectra of the reference $CaCO_3$ and the composite $CaCO_3$–Fe_3O_4 crystals. The crystallites have been found to be 31 ± 4 and 33 ± 12 nm for initial crystals (0 h) slightly decreasing after 20 h to 31 ± 10 and 25 ± 11 nm, respectively. This decrease can be possibly explained via the dissolution of a finite amount of vaterite crystallites and also by the partial recrystallization of vaterite phase to calcite. Moreover, the slightly smaller crystallite size of the composite $CaCO_3$–Fe_3O_4 vaterite (25 ± 11 nm) as compared to the reference $CaCO_3$ (31 ± 10 nm) can also be explained by the effect of nanoparticles accelerating the dissolution of calcium carbonate. The calcite crystallite sizes were 89 ± 12 nm for the composite and 75 ± 10 nm for the reference crystals after 40 h of incubation, when the samples were completely recrystallized to calcite.

The indicative peaks of Fe_3O_4 magnetite nanoparticles have not been found on the XRD spectra of $CaCO_3$–Fe_3O_4 crystals at any time. The probable reason is that the content of Fe_3O_4 nanoparticles is low as compared to the calcium carbonate (Table S1), so the stronger indicative peaks of vaterite and calcite dominate over refractive peaks of magnetite (if we consider the XRD spectra of Fe_3O_4 nanoparticles,[61,62] JCPDS-019-0629).

3.3. Loading/Release of the Protein. To use the composite $CaCO_3$–Fe_3O_4 vaterite as externally manipulated delivery systems with recrystallization-mediated release, the crystals should possess a porous internal structure suitable for

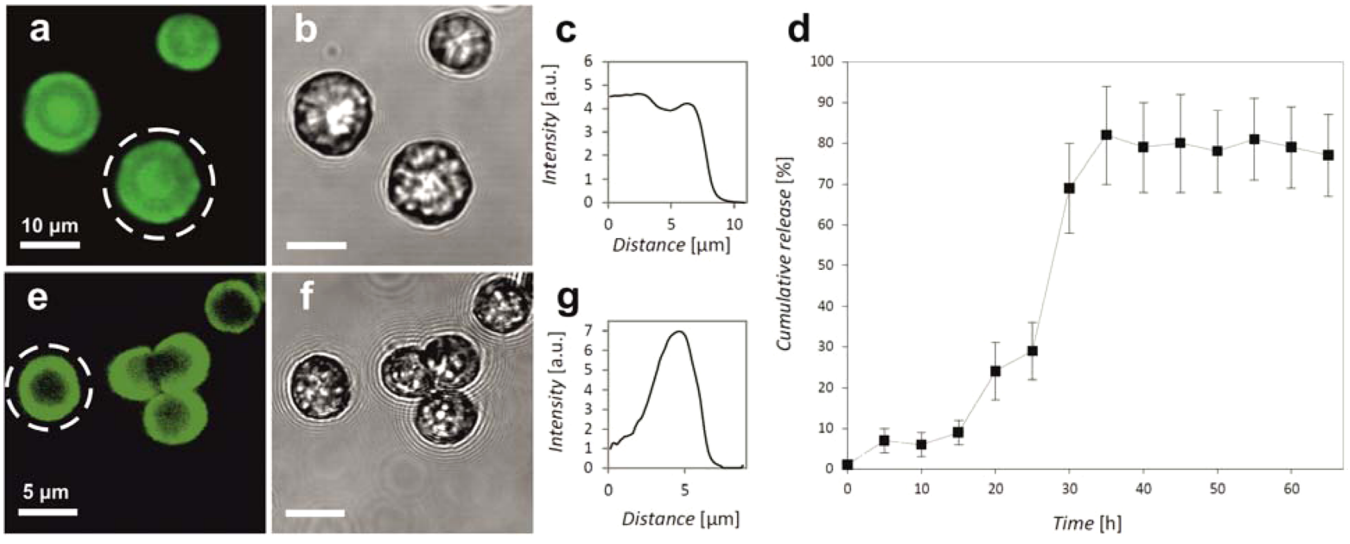

Figure 5. Fluorescent and optical transmittance images of the composite $CaCO_3$–Fe_3O_4 crystals (formed using colloid of 3 nm-sized Fe_3O_4 nanoparticles in water at concentration 1 mg mL^{-1}) loaded with FITC-lysozyme by (a,b) coprecipitation and (e,f) solvent evaporation approaches. Fluorescence radial profiles (c) and (g) correspond to the crystals indicated with the white interrupted circles in images (a) and (e), respectively. (d) Recrystallization-mediated release of FITC-lysozyme from $CaCO_3$–Fe_3O_4 crystals.

DOI: 10.1021/acsami.5b05848
ACS Appl. Mater. Interfaces 2015, 7, 21315–21325

loading of (bio)active molecules of interest. As demonstrated above by the SEM images, the magnetic $CaCO_3$−Fe_3O_4 crystals produced in this work have a highly porous inner structure (Figure 1g), similar to the common magnetite-free $CaCO_3$ vaterite (Figure 1e), well-known as an attractive system for templating of (bio)molecules.[14−17] To provide evidence that the integration into vaterite Fe_3O_4 nanoparticles did not cause the blocking of the pores (i.e., pores suitable for loading), FITC-lysozyme was encapsulated into the composite $CaCO_3$−Fe_3O_4 crystals (Figure 5). CLSM measurements revealed the homogeneous distribution of the additives over the internal vaterite structure (Figure 5a,c) when the protein was coprecipitated with salts. In the case when FITC-lysozyme was adsorbed into the pores of the already fabricated $CaCO_3$−Fe_3O_4 vaterite, protein molecules were mainly distributed in the near-surface area of the crystals (Figure 5d,f). This can most probably be explained by the sterical limitations of the lysozyme macromolecules (hydrodynamic radius about 2 nm)[63] to fill all of the pores over the crystals. Lysozyme did not permeate in the central part of vaterite (Figure 5d,f), demonstrating that the composite $CaCO_3$−Fe_3O_4 crystals have the internal structure denser (smaller pores) than the near-surface structure. In this way, both encapsulation approaches used (coprecipitation and solvent evaporation) have been shown to be successful in protein loading. This means that the internal and the near-surface pores of vaterite were not blocked by the precipitated Fe_3O_4 nanoparticles, so that the porous structure of the composite $CaCO_3$−Fe_3O_4 crystals can be used for the loading/release of (bio)molecules.

The FITC-lysozyme-loaded $CaCO_3$−Fe_3O_4 vaterite was used to investigate the recrystallization-mediated release of protein. As can be seen from the release profile (Figure 5d), after the first 15 h about 9 ± 3% of the encapsulated protein was found in the solution. The slow release observed is in line with the recrystallization kinetics of the composite $CaCO_3$−Fe_3O_4 crystals (a slow vaterite → calcite transformation for the first hours, Figure 3a) and can be explained by adsorption−desorption processes taking place on the crystal surfaces. Within the next 20 h (when all vaterite became calcite, Figure 3a), 70% of the encapsulated FITC-lysozyme was released into the solution; the curve reaches a plateau (Figure 5d). Finally, 82 ± 12% of the encapsulated protein was released into the media. Most probably, the rest protein macromolecules were captured between the "complex" calcite (as in Figure 2c) and electrostatically binded to the surfaces of calcite (isoelectric point of lysozyme 9.32).[64]

3.4. Recrystallization of the $CaCO_3$−Fe_3O_4 Vaterite Coated with $(PAH/PSS)_n$ Polyelectrolyte Shell. Experiments on the study of vaterite → calcite recrystallization kinetics were repeated for the reference $CaCO_3$ and the composite $CaCO_3$−Fe_3O_4 crystals covered with $(PAH/PSS)_n$ multilayers (n is 1,3,5) to reveal the influence of the polyelectrolyte shell on the vaterite stability. It is expected that the polyelectrolyte multilayer shell assembled on the vaterite crystals should inhibit the ionic exchange occurring in the near-surface region. Thus, the dissolution of vaterite followed by the growth of calcite phase should be prevented. Importantly, the deposited polyelectrolyte multilayers did not cause any loss of magnetic properties of the crystals.

In general terms, vaterite crystals covered with the $(PAH/PSS)_n$ shell were recrystallized to calcite by the same mechanism as uncoated as described in the previous section. However, as is evident from the recrystallization curves obtained (Figure 3b,c), the polyelectrolyte coating has dramatically affected the recrystallization kinetics for both $CaCO_3$ and $CaCO_3$−Fe_3O_4 crystals. Only the recrystallization kinetics of vaterite coated with a single $(PAH/PSS)_1$ polyelectrolyte bilayer is similar to that observed for the crystals without a shell (Figure 3). Most probably, this is because the shell consisted of a single bilayer is too thin to prevent the ion-exchange at the surface and, therefore, to affect the recrystallization kinetics. As is evident from the graphs (Figure 3b,c), the thicker is the polyelectrolyte shell, the slower is the vaterite → calcite recrystallization rate.

As supposed, the identically thick $(PAH/PSS)_5$ shells should provide similar recrystallization kinetics for $CaCO_3$ and $CaCO_3$−Fe_3O_4 crystals. However, the composite $CaCO_3$−Fe_3O_4/$(PAH/PSS)_5$ crystals were recrystallized to calcite much faster than the reference $CaCO_3$/$(PAH/PSS)_5$ vaterite (7 and 19 days, respectively). The only explanation is that Fe_3O_4 nanoparticles accelerate the vaterite → calcite recrystallization as described further.

SEM measurements revealed the presence of hollow $(PAH/PSS)_5$ polyelectrolyte capsules (Figure 6) after vaterite → calcite recrystallization had been completed. Most probably, the inner dissolution of carbonate core played a role because the surface of the $CaCO_3$−Fe_3O_4 crystals was well-protected by the LbL-assembled shell. As mentioned in the Experimental Section, Fe_3O_4 nanoparticles were stabilized with citric acid obtaining a negative electrokinetic potential (Table S1). As discussed earlier, when mixed with the salts, each Fe_3O_4 nanoparticle (or their clusters) became nucleation centers for ion precipitation (leading to aggregation and formation of the raspberry-vaterite). Most probably, the negatively charged Fe_3O_4 nanoparticles integrated into the internal $CaCO_3$ structure decreased the order of the crystal lattice (acting as defects or impurity atoms in the solid crystals). Therefore, they

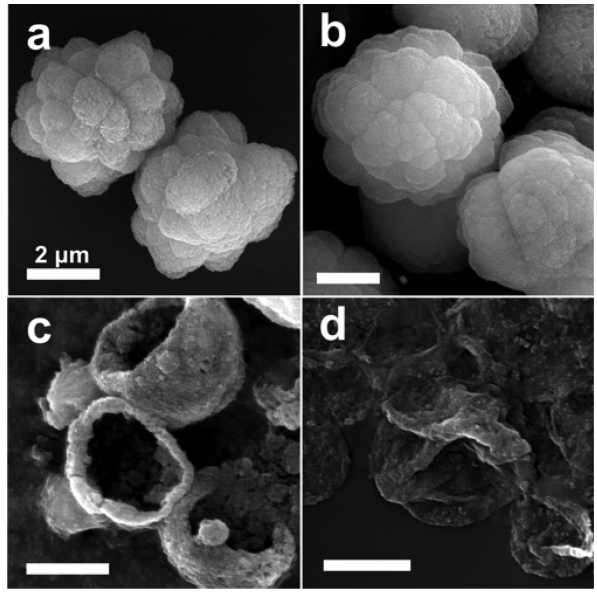

Figure 6. SEM images of $CaCO_3$−Fe_3O_4/$(PAH/PSS)_5$ crystals prepared using a suspension of Fe_3O_4 nanoparticles of an average size 70 nm and ζ-potential −27 mV: (a) $CaCO_3$−Fe_3O_4 crystals without polyelectrolyte shell, and $CaCO_3$−Fe_3O_4/$(PAH/PSS)_5$ crystals (b) after 1 day of incubation at 25 °C, (c) after 8 days, and (d) after 14 days. Scale bar is 2 μm for all of the images.

DOI: 10.1021/acsami.5b05848
ACS Appl. Mater. Interfaces 2015, 7, 21315−21325

can play a role in domains accelerating the internally initiated dissolution of calcium carbonate crystals. In this way, even coating of the surface with a polyelectrolyte shell (preventing the ion-exchange between the crystal surface and the solution) did not protect the composite $CaCO_3$–Fe_3O_4 vaterite from dissolution for the same time as the reference $CaCO_3$ vaterite (Figure 3b,c). Ions appearing inside the $CaCO_3$–Fe_3O_4 vaterite were released outside followed by the usual precipitation on the calcite surfaces (see the previous section). As a result, the empty $(PAH/PSS)_5$ polyelectrolyte capsules were kept after the vaterite dissolution had been completed (Figure 6), while calcite structures appeared in other places (Figure 2).

To summarize, two factors determine recrystallization of the LbL-coated $CaCO_3$–$Fe_3O_4/(PAH/PSS)_n$ vaterite: (i) thickness of the polyelectrolyte shell protecting the vaterite surface from the ion exchange-mediated dissolution, and (ii) content of Fe_3O_4 nanoparticles accelerating the inner dissolution of the composite $CaCO_3$–Fe_3O_4 crystals. This assumption is in a line with the recrystallization kinetics obtained for the composite $CaCO_3$–Fe_3O_4 and the reference $CaCO_3$ vaterite (Figures 3b,c).

Another important point is that the completely recrystallized $CaCO_3$–Fe_3O_4 crystals were not manipulated by the external field applied. Indeed, magnetic properties of the $CaCO_3$–Fe_3O_4 crystals were provided by Fe_3O_4 nanoparticles integrated into the mesoporous vaterite. Recrystallization from metastable vaterite to calcite caused the release of the previously integrated Fe_3O_4 nanoparticles, so that the magnetic properties were lost. The elementary composition analysis performed for the $CaCO_3$–$Fe_3O_4/(PAH/PSS)_n$ crystals (data not shown) revealed a total absence of iron in the structures completely recrystallized to calcite (such as in Figure 3f). At the same time, iron was presented in both not yet recrystallized $CaCO_3$–$Fe_3O_4/(PAH/PSS)_5$ vaterite (as in Figures 3a and 6a,b) and even in the empty $(PAH/PSS)_5$ polyelectrolyte microcapsules formed after calcium carbonate core dissolution (Figure 6c,d). This means that the thickness of the polyelectrolyte shell is high enough to keep the Fe_3O_4 nanoparticles inside, opening the ways to manipulate the external magnetic field not only with $CaCO_3$–$Fe_3O_4/(PAH/PSS)_n$ crystals but also with $(PAH/PSS)_n$ microcapsules formed after the crystal dissolution.

4. CONCLUSIONS

In this work, the coprecipitation approach was applied to prepare the composite $CaCO_3$–Fe_3O_4–protein vaterite. The crystals possess a characteristic raspberry-like shape, which enhances the active surface for higher loading capacity. Fe_3O_4 nanoparticles integrated into the mesoporous internal structure of $CaCO_3$–Fe_3O_4 provide the crystals with the ability to be manipulated in solutions of various viscosity by the external magnetic field applied. The recrystallization of the composite $CaCO_3$–Fe_3O_4 crystals results in the total loss of magnetic properties because all of the additives encapsulated in calcium carbonate (including both Fe_3O_4 nanoparticles and protein) are released from vaterite when recrystallized to nonporous calcite phase. In this way, the recrystallization-mediated release of the vaterite-encapsulated molecules can be performed.

The kinetics of vaterite → calcite recrystallization exhibits exponential behavior and depends on the ion-exchange between the dissolving vaterite phase and the growing calcite surfaces. Coating of $CaCO_3$–Fe_3O_4 crystals with the $(PAH/PSS)_n$ multilayers suppressed the ion-exchange and, thus, inhibited the vaterite → calcite recrystallization. The higher was the thickness of the polyelectrolyte shell, the slower was the recrystallization. The 5-bilayer shell extended the recrystallization time of the reference $CaCO_3$ vaterite from 34 h to 19 days. At the same time, Fe_3O_4 nanoparticles integrated into vaterite most probably reduced the order of the crystal lattice accelerating the inner dissolution of calcium carbonate. Thus, the recrystallization of the composite $CaCO_3$–Fe_3O_4 vaterite can be affected by the ion exchange going on the crystal surfaces, and by the content of Fe_3O_4 nanoparticles reducing the crystallinity of $CaCO_3$. Control over these factors can adjust the vaterite → calcite recrystallization kinetics, that is, the recrystallization-mediated release.

As a result of recrystallization of the composite $CaCO_3$–$Fe_3O_4/(PAH/PSS)_5$ crystals, the $(PAH/PSS)_5$ microcapsules were formed. After dissolution of calcium carbonate, Fe_3O_4 nanoparticles were found in the polyelectrolyte capsules. This allows for manipulation by an external magnetic field of both $CaCO_3$–Fe_3O_4 crystals and $(PAH/PSS)_5$ capsules self-assembled on the crystals. The simultaneous encapsulation of the protein and Fe_3O_4 nanoparticles into the calcium carbonate vaterite performed can open new ways to design multifunctional carriers with external manipulation for target delivery. The release kinetics of the encapsulated protein can be tuned by both the initial concentration of encapsulated Fe_3O_4 nanoparticles and the thickness of the assembled polyelectrolyte shell.

■ ASSOCIATED CONTENT

Supporting Information

The Supporting Information is available free of charge on the ACS Publications website at DOI: 10.1021/acsami.5b05848.

TEM images, DLS-measured values of size, and ζ-potential of the Fe_3O_4 nanoparticles fabricated; SEM images and characteristics of the composite $CaCO_3$–Fe_3O_4 crystals (average sizes, percentage of spherical and raspberry-vaterite crystals in samples, content of Fe_3O_4 nanoparticles in the composite crystals) for crystals fabricated using different Fe_3O_4 nanoparticles at various concentrations (PDF)

■ AUTHOR INFORMATION

Corresponding Author

*Phone: +49-177-5325483. E-mail: alenasergeeva@mail.ru, alena.sergeeva@izi-bb.fraunhofer.de.

Notes

The authors declare no competing financial interest.

■ ACKNOWLEDGMENTS

This work was partially supported the Alexander von Humboldt Foundation (AvH Fellowship and Sofja Kovalevskaja Program), by the Government of the Russian Federation (grant number 14.Z50.31.0004), and by grants from the RFBR (research projects No. 15-29-01172 and 14-12-00275). We thank Ilya Gorbachev (Saratov State University, Saratov, Russia) for the assistance in the preparation of the samples for SEM measurements.

■ REFERENCES

(1) Fajaroh, F.; Setyawan, H.; Widiyastuti, W.; Winardi, S. Synthesis of Magnetite Nanoparticles by Surfactant-Free Electrochemical Method in an Aqueous System *Adv. Adv. Powder Technol.* **2012**, *23*, 328–333.

DOI: 10.1021/acsami.5b05848
ACS Appl. Mater. Interfaces 2015, 7, 21315–21325

(2) Byrne, J. M.; Coker, V. S.; Cespedes, E.; Wincott, P. L.; Vaughan, D. J.; Pattrick; Richard, A. D.; van der Laan, G.; Arenholz, E.; Tuna, F.; Bencsik, M.; Lloyd, J. R.; Telling, N. D. Biosynthesis of Zinc Substituted Magnetite Nanoparticles with Enhanced Magnetic Properties. *Adv. Funct. Mater.* **2014**, *24*, 2518−2529.
(3) Gorin, D. A.; Portnov, S. A.; Inozemtseva, O. A.; Luklinska, Z.; Yashchenok, A. M.; Pavlov, A. M.; Skirtach, A. G.; Mohwald, H.; Sukhorukov, G. B. Magnetic/Gold Nanoparticle Functionalized Biocompatible Microcapsules with Sensitivity to Laser Irradiation. *Phys. Chem. Chem. Phys.* **2008**, *10*, 6899−6905.
(4) Finotelli, P. V.; Da Silva, D.; Sola-Penna, M.; Rossi, A. M.; Farina, M.; Andrade, L. R.; Takeuchi, A. Y.; Rocha-Leão, M. H. Microcapsules of Alginate/Chitosan Containing Magnetic Nanoparticles for Controlled Release of Insulin. *Colloids Surf., B* **2010**, *81*, 206−211.
(5) Haložan, D.; Riebentanz, U.; Brumen, M.; Donath, E. Polyelectrolyte Microcapsules and Coated $CaCO_3$ Particles as Fluorescence Activated Sensors in Flowmetry. *Colloids Surf., A* **2009**, *342*, 115−121.
(6) Demirors, A. F.; Pillai, P. P.; Kowalczyk, B.; Grzybowski, B. A. Colloidal Assembly Directed by Virtual Magnetic Moulds. *Nature* **2013**, *503*, 99−103.
(7) Yamamoto, M.; Yasukawa, T.; Suzuki, M.; Kosuge, S.; Shiku, H.; Matsue, T.; Mizutani, F. Patterning with Particles Using Three-Dimensional Interdigitated Array Electrodes with Negative Dielectrophoresis and its Application to Simple Immunosensing: Electrochemical Frontiers in Global Environment and Energy. *Electrochim. Acta* **2012**, *82*, 35−42.
(8) Sergeeva, A.; Gorin, D.; Volodkin, D. Polyelectrolyte Microcapsule Arrays: Preparation and Biomedical Applications. *BioNanoSci.* **2014**, *4*, 1−14.
(9) Parakhonskiy, B. V.; Foss, C.; Carletti, E.; Fedel, M.; Haase, A.; Motta, A.; Migliaresi, C.; Antolini, R. Tailored Intracellular Delivery via a Crystal Phase Transition in 400 nm Vaterite Particles. *Biomater. Sci.* **2013**, *1*, 1273−1281.
(10) Volodkin, D. V.; Petrov, A. I.; Prevot, M.; Sukhorukov, G. B. Matrix Polyelectrolyte Microcapsules: New System for Macromolecule Encapsulation. *Langmuir* **2004**, *20*, 3398−3406.
(11) Volodkin, D. V.; Schmidt, S.; Fernandes, P.; Larionova, N. I.; Sukhorukov, G. B.; Duschl, C.; Möhwald, H.; Klitzing, R. von. One-Step Formulation of Protein Microparticles with Tailored Properties: Hard Templating at Soft Conditions. *Adv. Funct. Mater.* **2012**, *22*, 1914−1922.
(12) Sukhorukov, G. B.; Volodkin, D. V.; Gunther, A. M.; Petrov, A. I.; Shenoy, D. B.; Mohwald, H. Porous Calcium Carbonate Microparticles as Templates for Encapsulation of Bioactive Compounds. *J. Mater. Chem.* **2004**, *14*, 2073−2081.
(13) Trushina, D. B.; Bukreeva, T. V.; Kovalchuk, M. V.; Antipina, M. N. $CaCO_3$ Vaterite Microparticles for Biomedical and Personal Care Applications. *Mater. Sci. Eng., C* **2014**, *45*, 644−658.
(14) Schmidt, S.; Volodkin, D. Microparticulate Biomolecules by Mild $CaCO_3$ Templating. *J. Mater. Chem. B* **2013**, *1*, 1210−1218.
(15) Behra, M.; Schmidt, S.; Hartmann, J.; Volodkin, D. V.; Hartmann, L. Synthesis of Porous PEG Microgels Using $CaCO_3$ Microspheres as Hard Templates. *Macromol. Rapid Commun.* **2012**, *33*, 1049−1054.
(16) Schmidt, S.; Behra, M.; Uhlig, K.; Madaboosi, N.; Hartmann, L.; Duschl, C.; Volodkin, D. Mesoporous Protein Particles Through Colloidal $CaCO_3$ Templates. *Adv. Funct. Mater.* **2013**, *23*, 116−123.
(17) Volodkin, D. $CaCO_3$ Templated Micro-Beads and -Capsules for Bioapplications. *Adv. Colloid Interface Sci.* **2014**, *207*, 306−324.
(18) Svenskaya, Y.; Parakhonskiy, B.; Haase, A.; Atkin, V.; Lukyanets, E.; Gorin, D.; Antolini, R. Anticancer Drug Delivery System Based on Calcium Carbonate Particles Loaded with a Photosensitizer. *Biophys. Chem.* **2013**, *182*, 11−15.
(19) Peng, C.; Zhao, Q.; Gao, C. Sustained Delivery of Doxorubicin by Porous $CaCO_3$ and Chitosan/Alginate Multilayers-Coated $CaCO_3$ Microparticles. *Colloids Surf., A* **2010**, *353*, 132−139.
(20) Volodkin, D. V.; von Klitzing, R.; Möhwald, H. Pure Protein Microspheres by Calcium Carbonate Templating. *Angew. Chem., Int. Ed.* **2010**, *49*, 9258−9261.
(21) Schmidt, S.; Uhlig, K.; Duschl, C.; Volodkin, D. Stability and Cell Uptake of Calcium Carbonate Templated Insulin Microparticles. *Acta Biomater.* **2014**, *10*, 1423−1430.
(22) Parakhonskiy, B. V.; Svenskaya, Y. I.; Yashchenok, A. M.; Fattah, H. A.; Inozemtseva, O. A.; Tessarolo, F.; Antolini, R.; Gorin, D. A. Size Controlled Hydroxyapatite and Calcium Carbonate Particles: Synthesis and Their Application as Templates for SERS Platform. *Colloids Surf., B* **2014**, *118*, 243−248.
(23) Kulak, A. N.; Semsarilar, M.; Kim, Y.-Y.; Ihli, J.; Fielding, L. A.; Cespedes, O.; Armes, S. P.; Meldrum, F. C. One-Pot Synthesis of an Inorganic Heterostructure: Uniform Occlusion of Magnetite Nanoparticles within Calcite Single Crystals. *Chem. Sci.* **2014**, *5*, 738−743.
(24) Fakhrullin, R. F.; Bikmullin, A. G.; Nurgaliev, D. K. Magnetically Responsive Calcium Carbonate Microcrystals. *ACS Appl. Mater. Interfaces* **2009**, *1*, 1847−1851.
(25) Shchukin, D. G.; Sukhorukov, G. B.; Price, R. R.; Lvov, Y. M. Halloysite Nanotubes as Biomimetic Nanoreactors. *Small* **2005**, *1*, 510−513.
(26) Ford, W. E.; Yasuda, A.; Wessels, J. M. Microcrystalline Composite Particles of Carbon Nanotubes and Calcium Carbonate. *Langmuir* **2008**, *24*, 3479−3485.
(27) Petrov, A. I.; Volodkin, D. V.; Sukhorukov, G. B. Protein-Calcium Carbonate Coprecipitation: a Tool for Protein Encapsulation. *Biotechnol. Prog.* **2005**, *21*, 918−925.
(28) Decher, G.; Hong, J. D. Buildup of Ultrathin Multilayer Films by a Self-Assembly Process: II. Consecutive Adsorption of Anionic and Cationic Bipolar Amphiphiles and Polyelectrolytes on Charged Surfaces. *Ber. Bunsenges. Phys. Chem.* **1991**, *95*, 1430−1434.
(29) Marchenko, I.; Yashchenok, A.; German, S.; Inozemtseva, O.; Gorin, D.; Bukreeva, T.; Mohwald, H.; Skirtach, A. Polyelectrolytes: Influence on Evaporative Self-Assembly of Particles and Assembly of Multilayers with Polymers, Nanoparticles and Carbon Nanotubes. *Polymers* **2010**, *2*, 690−708.
(30) Bukreeva, T. V.; Orlova, O. A.; Sulyanov, S. N.; Grigoriev, Y. V.; Dorovatovskiy, P. V. A New Approach to Modification of Polyelectrolyte Capsule Shells by Magnetite Nanoparticles. *Crystallogr. Rep.* **2011**, *56*, 880−883.
(31) Luo, R.; Venkatraman, S. S.; Neu, B. Layer-by-Layer Polyelectrolyte−Polyester Hybrid Microcapsules for Encapsulation and Delivery of Hydrophobic Drugs. *Biomacromolecules* **2013**, *14*, 2262−2271.
(32) Yashchenok, A. M.; Borisova, D.; Parakhonskiy, B. V.; Masic, A.; Pinchasik, B.; Möhwald, H.; Skirtach, A. G. Nanoplasmonic Smooth Silica Versus Porous Calcium Carbonate Bead Biosensors for Detection of Biomarkers. *Ann. Phys.* **2012**, *524*, 723−732.
(33) Skirtach, A. G.; Dejugnat, C.; Braun, D.; Susha, A. S.; Rogach, A. L.; Parak, W. J.; Möhwald, H.; Sukhorukov, G. B. The Role of Metal Nanoparticles in Remote Release of Encapsulated Materials. *Nano Lett.* **2005**, *5*, 1371−1377.
(34) Goss, S. L.; Lemons, K. A.; Kerstetter, J. E.; Bogner, R. H. Determination of Calcium Salt Solubility with Changes in pH and P_{CO2}, Simulating Varying Gastrointestinal Environments. *J. Pharm. Pharmacol.* **2007**, *59*, 1485−1492.
(35) Brečević, L.; Kralj, D. On Calcium Carbonates: from Fundamental Research to Application. *Croat. Chem. Acta* **2007**, *80*, 467−484.
(36) Xue, X.; Furlani, E. P. Template-Assisted Nano-Patterning of Magnetic Core-Shell Particles in Gradient Fields. *Phys. Chem. Chem. Phys.* **2014**, *16*, 13306−13317.
(37) Ogino, T.; Suzuki, T.; Sawada, K. The Formation and Transformation Mechanism of Calcium Carbonate in Water. *Geochim. Cosmochim. Acta* **1987**, *51*, 2757−2767.
(38) Ogino, T.; Suzuki, T.; Sawada, K. The Rate and Mechanism of Polymorphic Transformation of Calcium Carbonate in Water. *J. Cryst. Growth* **1990**, *100*, 159−167.

DOI: 10.1021/acsami.5b05848
ACS Appl. Mater. Interfaces 2015, 7, 21315−21325

(39) Berdonosov, S. S.; Znamenskaya, I. V.; Melikhov, I. V. Mechanism of the Vaterite-to-Calcite Phase Transition under Sonication. *Inorg. Mater.* **2005**, *41*, 1308−1312.
(40) Rodriguez-Blanco, J. D.; Shaw, S.; Benning, L. G. The Kinetics and Mechanisms of Amorphous Calcium Carbonate (ACC) Crystallization to Calcite, via Vaterite. *Nanoscale* **2011**, *3*, 265−271.
(41) Sarkar, A.; Mahapatra, S. Mechanism of Unusual Polymorph Transformations in Calcium Carbonate: Dissolution-Recrystallization vs Additive-Mediated Nucleation. *J. Chem. Sci.* **2012**, *124*, 1399−1404.
(42) Parakhonskiy, B. V.; Haase, A.; Antolini, R. Sub-Micrometer Vaterite Containers: Synthesis, Substance Loading, and Release. *Angew. Chem., Int. Ed.* **2012**, *51*, 1195−1197.
(43) Volodkin, D.; Klitzing, R. von. Competing Mechanisms in Polyelectrolyte Multilayer Formation and Swelling: Polycation−Polyanion Pairing vs. Polyelectrolyte−Ion Pairing. *Curr. Opin. Colloid Interface Sci.* **2014**, *19*, 25−31.
(44) Pechenkin, M. A.; Mohwald, H.; Volodkin, D. V. pH- and Salt-Mediated Response of Layer-by-Layer Assembled PSS/PAH Microcapsules: Fusion and Polymer Exchange. *Soft Matter* **2012**, *8*, 8659−8665.
(45) Massart, R. Preparation of Aqueous Magnetic Liquids in Alkaline and Acidic Media. *IEEE Trans. Magn.* **1981**, *17*, 1247−1248.
(46) German, S. V.; Inozemtseva, O. A.; Navolokin, N. A.; Pudovkina, E. E.; Zuev, V. V.; Volkova, E. K.; Bucharskaya, A. B.; Pleskova, S. N.; Maslyakova, G. N.; Gorin, D. A. Synthesis of Magnetite Hydrosols and Assessment of Their Impact on Living Systems at the Cellular and Tissue Levels Using MRI and Morphological Investigation. *Nanotechnol. Russ.* **2013**, *8*, 573−580.
(47) German, S. V.; Inozemtseva, O. A.; Markin, A. V.; Metvalli, K.; Khomutov, G. B.; Gorin, D. A. Synthesis of Magnetite Hydrosols in Inert Atmosphere. *Colloid J.* **2013**, *75*, 483−486.
(48) Le Bail, A.; Ouhenia, S.; Chateigner, D. Microtwinning Hypothesis for a More Ordered Vaterite Model. *Powder Diffr.* **2011**, *26*, 16−21.
(49) Sitepu, H. Texture and Structural Refinement Using Neutron Diffraction Data from Molybdite (MoO_3) and Calcite ($CaCO_3$) Powders and a Ni-Rich $Ni_{50.7}Ti_{49.30}$ Alloy. *Powder Diffr.* **2009**, *24*, 315−326.
(50) Scherrer, P. Bestimmung der Inneren Struktur und der Größe von Kolloidteilchen Mittels Röntgenstrahlen Kolloidchemie Ein Lehrbuch. *Chemische Technologie in Einzeldarstellungen*; Springer: Berlin, Heidelberg, 1912; pp 387−409.
(51) Scherrer, P. Bestimmung der Größe und der inneren Struktur von Kolloidteilchen mittels Röntgenstrahlen. *Göttinger Nachr.* **1918**, *2*, 98−100.
(52) Yu, J.; Lei, M.; Cheng, B.; Zhao, X. Facile Preparation of Calcium Carbonate Particles with Unusual Morphologies by Precipitation Reaction. *J. Cryst. Growth* **2004**, *261*, 566−570.
(53) Bots, P.; Benning, L. G.; Rodriguez-Blanco, J.-D.; Roncal-Herrero, T.; Shaw, S. Mechanistic Insights into the Crystallization of Amorphous Calcium Carbonate (ACC). *Cryst. Growth Des.* **2012**, *12*, 3806−3814.
(54) Gebauer, D.; Volkel, A.; Colfen, H. Stable Prenucleation Calcium Carbonate Clusters. *Science* **2008**, *322*, 1819−1822.
(55) Chien, W.-C.; Lee, C.-C.; Tai, C. Y. Heterogeneous Nucleation Rate of Calcium Carbonate Derived from Induction Period. *Ind. Eng. Chem. Res.* **2007**, *46*, 6435−6441.
(56) Trushina, D. B.; Sulyanov, S. N.; Bukreeva, T. V.; Kovalchuk, M. V. Size Control and Structure Features of Spherical Calcium Carbonate Particles. *Crystallogr. Rep.* **2015**, *60*, 570−577.
(57) Guo, X.; Liu, L.; Wang, W.; Zhang, J.; Wang, Y.; Yu, S.-H. Controlled Crystallization of Hierarchical and Porous Calcium Carbonate Crystals Using Polypeptide Type Block Copolymer as Crystal Growth Modifier in a Mixed Solution. *CrystEngComm* **2011**, *13*, 2054−2061.
(58) Ni, M.; Ratner, B. D. Differentiating Calcium Carbonate Polymorphs by Surface Analysis Techniques—an XPS and TOF-SIMS Study. *Surf. Interface Anal.* **2008**, *40*, 1356−1361.
(59) Kontoyannis, C. G.; Vagenas, N. V. Calcium Carbonate Phase Analysis Using XRD and FT-Raman Spectroscopy. *Analyst* **2000**, *125*, 251−255.
(60) Antao, S. M.; Hassan, I. The Orthorhombic Structure of $CaCO_3$, $SrCO_3$, $PbCO_3$ and $BaCO_3$: Linear Structural Trends. *Can. Mineral.* **2009**, *47*, 1245−1255.
(61) Prakash, R.; Fanselau, K.; Ren, S.; Kumar Mandal, T.; Kubel, C.; Hahn, H.; Fichtner, M. A Facile Synthesis of a Carbon-Encapsulated Fe_3O_4 Nanocomposite and its Performance as Anode in Lithium-Ion Batteries. *Beilstein J. Nanotechnol.* **2013**, *4*, 699−704.
(62) Fang, M.; Volotinen, T. T.; Kulkarni, S. K.; Belova, L.; Rao, K. V. Effect of Embedding Fe_3O_4 Nanoparticles in Silica Spheres on the Optical Transmission Properties of Three-Dimensional Magnetic Photonic Crystals. *J. Appl. Phys.* **2010**, *108*, 103501.
(63) Grigsby, J. J.; Blanch, H. W.; Prausnitz, J. M. Diffusivities of Lysozyme in Aqueous $MgCl_2$ Solutions from Dynamic Light-Scattering Data: Effect of Protein and Salt Concentrations. *J. Phys. Chem. B* **2000**, *104*, 3645−3650.
(64) Hernandez-Hernandez, A.; Rodriguez-Navarro, A. B.; Gomez-Morales, J.; Jimenez-Lopez, C.; Nys, Y.; Garzia-Ruiz, J. M. Influence of Model Globular Proteins with Different Isoelectric Points on the Precipitation of Calcium Carbonate. *Cryst. Growth Des.* **2008**, *8*, 1495−1502.

DOI: 10.1021/acsami.5b05848
ACS Appl. Mater. Interfaces 2015, 7, 21315−21325